TABLE 1. Star Counts

Radius	Number of stars per square arcsecond		
(arcsec)	$18.75 < V < 20.25$	$20.25 < V < 21.75$	$21.75 < V < 23.25$
0.50	11.3 ± 2.8	$\cdots$	$\cdots$
1.26	9.3 ± 2.5	$\cdots$	$\cdots$
2.00	4.6 ± 1.1	6.1 ± 1.3	$\cdots$
3.16	4.2 ± 0.6	4.0 ± 0.6	1.5 ± 0.4
5.01	2.9 ± 0.3	3.2 ± 0.4	2.3 ± 0.3
7.94	2.0 ± 0.3	2.4 ± 0.3	0.9 ± 0.2
12.59	1.5 ± 0.6	1.3 ± 0.5	2.1 ± 0.7

TABLE 2. Luminosity Functions

| V | (# stars) / (square arcmin) (V magnitude) | |
	$0'' < r < 6''$	$6'' < r < 12''$
19.0	$(0.72 \pm 0.13) \times 10^4$	$(2.44 \pm 0.71) \times 10^3$
19.5	$(1.24 \pm 0.16) \times 10^4$	$(5.87 \pm 1.04) \times 10^3$
20.0	$(1.20 \pm 0.16) \times 10^4$	$(6.83 \pm 1.14) \times 10^3$
20.5	$(1.05 \pm 0.15) \times 10^4$	$(7.01 \pm 1.14) \times 10^3$
21.0	$(1.23 \pm 0.17) \times 10^4$	$(6.07 \pm 1.11) \times 10^3$
21.5	$(1.01 \pm 0.16) \times 10^4$	$(3.70 \pm 0.85) \times 10^3$
22.0	$(1.02 \pm 0.18) \times 10^4$	$(4.74 \pm 1.03) \times 10^3$
22.5	$(0.61 \pm 0.14) \times 10^4$	$(1.83 \pm 0.65) \times 10^3$
23.0	$\cdots$	$(2.28 \pm 0.81) \times 10^3$

TABLE 3. Mass Functions

| Mass | (# stars) / (square arcsec) ($M_\odot$) | |
(M_⊙)	$0'' < r < 6''$	$6'' < r < 12''$
0.76	52.45 ± 0.19	17.86 ± 0.10
0.74	63.89 ± 0.22	30.18 ± 0.14
0.71	50.52 ± 0.22	28.76 ± 0.16
0.67	38.32 ± 0.21	25.63 ± 0.16
0.63	43.95 ± 0.24	21.62 ± 0.15
0.59	37.05 ± 0.22	13.53 ± 0.12
0.55	36.28 ± 0.25	16.88 ± 0.14
0.51	19.58 ± 0.20	5.90 ± 0.09
0.47	$\cdots$	6.22 ± 0.11

TABLE 4. Corners of Imaged Area

FOC pixel coordinates		J2000 coordinates	
x	y	N	E
-25.4	314.7	$3\rlap{.}''26$	$3\rlap{.}''14$
-13.4	-182.3	$-2\rlap{.}''15$	$-1\rlap{.}''51$
19.6	-184.3	$-1\rlap{.}''87$	$-1\rlap{.}''89$
45.6	-679.6	$-7\rlap{.}''13$	$-6\rlap{.}''68$
286.4	-683.3	$-4\rlap{.}''99$	$-9\rlap{.}''39$
495.2	-678.7	$-3\rlap{.}''04$	$-11\rlap{.}''67$
475.6	-185.3	$2\rlap{.}''26$	$-6\rlap{.}''96$
438.6	-185.3	$1\rlap{.}''93$	$-6\rlap{.}''55$
432.6	314.7	$7\rlap{.}''43$	$-1\rlap{.}''94$

Notes to Table 4.

Listed coordinates are relative to the cluster center, which is located at $(50.4, 195.3)$ in pixel coordinates (the coordinate system of the uppermost FOC pointing in Fig. 1), and at $(21^{\mathrm{h}}40^{\mathrm{m}}22\rlap{.}^{\mathrm{s}}164, -23°10'47\rlap{.}''12)$ in J2000 coordinates.

TABLE 5A. King-model parameters

r_c	$0.036\,\mathrm{pc} = 1''$
r_t	$28.5\,\mathrm{pc} = 13.'2$
W_0	21.9
Total cluster mass	$6.42 \times 10^4\ M_\odot$
Total number of stars	1.50×10^5
ρ_0	$8.45 \times 10^5 M_\odot/\mathrm{pc}^3$

Notes to Table 5a.

Entries in this table refer to cluster model parameters as defined by Gunn & Griffin (1979).

TABLE 5B. King-model mass function

Mass $(M_\odot)$	Fraction of total mass	Fraction of central mass density
0.779	0.0112	1.136×10^{-2}
0.768	0.0227	2.060×10^{-2}
0.749	0.0305	2.262×10^{-2}
0.722	0.0381	2.117×10^{-2}
0.689	0.0507	1.972×10^{-2}
0.651	0.0616	1.583×10^{-2}
0.612	0.0686	1.149×10^{-2}
0.574	0.0611	6.747×10^{-3}
0.535	0.0544	3.927×10^{-3}
0.492	0.0536	2.439×10^{-3}
0.441	0.0563	1.498×10^{-3}
0.375	0.0555	7.617×10^{-4}
0.301	0.0782	5.401×10^{-4}
0.246	0.0647	2.814×10^{-4}
0.206	0.0506	1.619×10^{-4}
0.178	0.0329	8.607×10^{-5}
0.550	0.1961	1.667×10^{-2}
1.330	0.0138	8.441×10^{-1}

Mass Segregation and Equipartition of Energy in Two Globular Clusters with Central Density Cusps[1]

Craig Sosin

Astronomy Department, University of California, Berkeley, CA 94720-3411

E-mail: csosin@astro.berkeley.edu

ABSTRACT

We begin by presenting the analysis of a set of deep B- and V-band images of the central density cusp of the globular cluster M30 (NGC 7099), taken with the Faint Object Camera aboard the *Hubble Space Telescope.* These images are the first to resolve lower-mass main-sequence stars in the cluster's central $10''$. From the positions of individual stars, we measure an improved position for the cluster center; this new position is $2\rlap{.}''6$ from the previously known position. We find no evidence of a "flat", constant-surface-density core; however, the data do not rule out the presence of a core of radius up to $1\rlap{.}''9$ (95% confidence level). We measure a logarithmic cusp slope ($d\log\sigma/d\log r$) of -0.76 ± 0.07 (1-sigma) for stars with masses between 0.69 and $0.76 M_\odot$, and -0.82 ± 0.11 for stars with masses between 0.57 and $0.69 M_\odot$. We also compare the overall mass function (MF) of the cluster cusp with the MF of a field at $r = 4\rlap{.}'6$ (near the cluster half-mass radius). The observed degree of mass segregation is well matched by the predictions of an isotropic, multimass King model.

We then use the Jeans equation to compare the structure of M30 with that of M15, another cusped cluster, using data from this and a previous paper. We find that M30 is very close to achieving equipartition of energy between stellar species, at least over the observed range in mass and radius, while M15 is not. This difference may be a result of the longer relaxation time in the observed field in M15. The data also suggest that the degree of mass segregation within the two cluster cusps is smaller than one would expect from the measurements at larger radius. If so, this phenomenon might be the result of gravothermal oscillations, of centrally-concentrated populations of binaries, or of a $\sim 10^3 M_\odot$ black hole in one or more clusters.

Subject headings: globular clusters—stellar systems (kinematics, dynamics)

---

1. Introduction

Theoretical arguments, computational simulations, and high-resolution observations have all shown that the cores of high-concentration globular clusters collapse, on timescales comparable to the Hubble time. The result of this collapse is a power-law density cusp, believed to be supported against further collapse by the transfer of energy out of binary stars through stellar encounters (see the reviews in Djorgovski & Meylan 1993a and Hut & Makino 1996). With the observation of density cusps in $\sim 20\%$ of Galactic globulars (Djorgovski & King 1986, Lugger *et al.* 1995), core collapse has become the standard model of cluster dynamical evolution; alternative explanations for the existence of the cusps, such as the presence of a central black hole (Bahcall & Wolf 1976, 1977) are now less favored. Recently, the repair of the *Hubble Space Telescope (HST)* has allowed faint stars in cluster cusps to be observed for the first time, and has made detailed tests of these models possible.

In a previous paper (Sosin & King 1997, hereafter Paper I), we presented our analysis of several *HST*/Faint Object Camera (FOC) images of the central cusp of the cluster M15. Here, we begin by examining a similar set of images of the cluster M30 (NGC 7099). As before, our primary goals are to investigate the distribution of stars of different mass, and to use those distributions to test theories of the structure and evolution of globular clusters. After presenting the M30 data, we compare the two clusters, and suggest some possible reasons for the differences between them that we observe.

Like M15, M30 is a cusped—presumably post-core-collapse—cluster, with low metal abundance ([Fe/H] = −2.1) and advanced age. *HST*/WFPC2 imaging has recently shown that M15 and M30 have nearly identical global mass functions (Piotto, Cool, & King 1997), suggesting that the pair were formed in very similar circumstances. However, M30 has only about one-third the mass of M15, and a shorter half-mass relaxation time (Djorgovski 1993).

2. The M30 Data

2.1. Observations

M30 was observed by *HST* in December 1994, with the COSTAR optical correction system in place. Two $\sim 7'' \times 7''$ FOC fields were observed near the cluster center on 5 December, and an additional FOC field at a radius of $21''$ was observed two days later. This latter field unfortunately includes a bright giant that saturated a large portion of the FOC detector; that fact plus the lower stellar density at $r = 21''$ imply that there are too few stars in the field to measure a meaningful luminosity function. For the rest of this paper we consider only the two inner fields.

Each of these two fields was observed through the FOC equivalents of B and V filters (F430W and F480LP, respectively) for a total of ~ 4000 seconds. Their combined V image is shown in Figure 1. The first field was intended to be positioned so that the cluster center would be near

its midpoint, however, errors in the previously known position of the center led to the center appearing near the left edge of the image. The second field is about $7''$ from the first; the two overlap by only a few pixels along one edge. Together, the two span a radial range from the cluster center out to $r \simeq 12''$, far enough out that the images show the cusp's entire radial extent.

The FOC detector saturates at high count rates, rather than at high numbers of counts, so saturation of stellar images is often a problem in FOC images. The large, crescent-shaped "objects" in Fig. 1 are saturated giants; their odd shape is a result of hysteresis effects in the detector. In addition, many of the brightest main-sequence stars in the images have nonlinear pixels in their centers, especially in the B image. In Paper I, the extreme crowding of saturated stars made the B images of the center of M15 difficult to work with, but here, both the B and V images of M30 are usable.

The M30 images were also taken shortly after the FOC was turned on, after having been off for several days. Because the detector was still warming up, the plate scale changed slowly over the course of the observations. This effect is especially pronounced for the V image of the second field (which was actually the first to be taken), in which stars are somewhat distorted near the image corners. However, since this distortion appears in the same parts of the images in which the FOC's flatfielding and geometric correction are poor even under normal conditions, it affects the photometric accuracy very little.

2.2. Data Reduction

We used the same procedure as in Paper I to obtain positions and magnitudes of stars in the two M30 fields. We refer the reader to the previous paper for an in-depth description of the method. Essentially, we run DAOPHOT and ALLSTAR (Stetson 1987, 1992) on the image twice; the results from the first pass are used to subtract features of the FOC point-spread function that are easily confused with faint stars (e.g., intersections of diffraction spikes with Airy rings). The second pass, which uses this "ring-subtracted" image as input, can then reliably find stars at fainter magnitudes. The lower stellar density in M30 made the third pass from Paper I, which was used to split close stellar blends, unnecessary.

We calibrated our photometry to standard FOC instrumental magnitudes using photometric parameters provided by the STScI pipeline, and then transformed to Johnson B and V, as described in Paper I. Since the metal abundances of M15 and M30 are so similar, we used the same color equations as in the previous paper (King, Anderson, & Sosin 1994).

As in Paper I, the points on the $(V, B - V)$ diagram came out somewhat bluer and/or fainter than points on ground-based CMDs of the same cluster. We have no way of knowing whether the problem is in the FOC calibration or in the color equations used to transform to B and V. The discrepancy could be resolved in more than one way: for example, the B magnitudes could be made fainter by 0.15 mag, or the V magnitudes could be made brighter by 0.12 mag. Alternatively,

both magnitudes could change by some larger quantity. Since the stars being observed are fainter than any observed previously in the cusp, we have no other way to calibrate the photometry, and must accept the nominal FOC calibration as being approximately correct. (The mass functions to be measured later are affected little by a shift of 0.1 mag.)

The CMD of the M30 cusp is shown in Figure 2. The dashed line in the figure is the main-sequence ridgeline observed from the ground (at larger radius) by Bolte (1987), while the solid line is the ([Fe/H] $= -2.03$, $t = 16$ Gyr) isochrone of Bergbusch & VandenBerg (1992, hereafter BV92). (Later, we will use the mass–luminosity relation associated with this isochrone.) The observed B magnitudes have been adjusted 0.15 mag fainter in order to match the ground-based ridgeline. The redward deviation of the FOC points from the isochrone at the bright end is due to the onset of nonlinearity in the B image. The V magnitudes of the stars shown are nearly unaffected by nonlinearity.

We then ran artificial-star experiments to determine the completeness of the star-counting as a function of magnitude and position. About 10^4 artificial stars were added to each of the two fields (64 stars were added per experiment), with randomly selected V magnitudes, and B magnitudes chosen to put the artificial star on the main-sequence ridgeline. The images were then re-reduced in the same automated way as the originals, and the output lists were examined to see which artificial stars were recovered. In addition, we also recorded the input and output magnitudes of any real neighbors of the added artificial stars.

The counts of stars of moderate magnitude ($V \simeq 21$) are nearly complete over the entire radial range. The few stars that are not detected at these magnitudes are missed because of the obvious bright stars seen in Fig. 1. The photometry becomes more and more incomplete at fainter magnitudes, before giving out at $V \simeq 23$, as faint stars become lost in the fluctuations of the background light (from sky and bright-star halos). A comparison of magnitudes of nonrecovered artificial stars with their real-star neighbors revealed that blends of stars of nearly equal magnitude are much less common here than in the M15 images. Thus, we do not need to worry about the uncertainties in completeness corrections that would result from those blends (see Paper I).

It is likely that some of the stars in Fig. 2 are binaries. Binaries consisting of a main-sequence (MS) star and a dark stellar remnant (e.g., a neutron star or faint white dwarf) are indistinguishable from single MS stars in the CMD; however, the combined mass of the two binary components is considerably larger than the mass of a single star with the same magnitude. If the fraction of stars that are binaries is large, then the analysis of the dynamics becomes more difficult, since we then cannot rely on the mass-luminosity relation given by the BV92 isochrone. Binaries composed of two MS stars, on the other hand, would appear above the MS ridgeline by up to 0.75 mag. Rubenstein & Bailyn (1997) have recently observed a high ($> 15\%$) MS binary fraction in the cusp of NGC 6752, a cluster whose dynamical parameters are similar to those of M30. However, in M30, there does not appear to be a large number of nearly equal-mass MS–MS binaries, at least in the $21 < V < 22$ range where they would be easily distinguished from single

stars (see Fig. 2). But, the photometric precision of the FOC is not really sufficient to distinguish MS–MS binaries from single MS stars over a very wide range of magnitude, so this conclusion is tentative.

Individual stellar magnitudes and positions, and the detailed results of the artificial-star experiments, are available from the author.

3. Stellar Distributions in M30

3.1. The Cluster Center

The position of the center of M30 is not known to within an accuracy of several arcseconds, as was made clear by the near-mistargeting of our images. We need an accurate position for the center in order to measure the cluster's surface-density profile.

The cluster center is usually taken to be a point of maximum symmetry of the stellar density; thus, an accurate measurement of its position requires an image of a large surrounding region. We cannot find a point of symmetry from our FOC images alone, since the general area in which the center is located appears near their edge. However, Yanny et $al.$ (1994) took a set of HST/WFPC2 images of the M30 cusp in April 1994. Their Planetary Camera (PC) image covers a larger $20'' \times 20''$ area around the cluster center, although the images are not as deep as our FOC images.

We obtained the Yanny et $al.$ V-band PC image from the HST Archive, and used it to measure an improved position for the center as follows. We first reduced the image using DAOPHOT and ALLSTAR and a rough point-spread function. We then selected a magnitude cutoff, guessed a prospective center, and then found the number-weighted centroid of the positions of the stars within some radius r of that center. We used the result of that measurement as the next guess for the center's position, and iterated until the position converged, which generally took only two or three iterations. We tried a variety of magnitude cutoffs ($V = 18$ to 19) and radii r (5 to $10''$).

The position of the center measured with various combinations of parameters varied by $0\rlap{.}''5$ or so. We took a typical position in the middle of the range as our adopted cluster center. We then transferred its position to a position on the FOC image using a transformation derived from the positions of several bright stars, and finally to standard coordinates using the STSDAS $xy2rd$ task. The position of the center, in J2000 coordinates, is ($21^{\mathrm{h}}40^{\mathrm{m}}22\rlap{.}^{\mathrm{s}}164, -23°10'47\rlap{.}''12$), and is marked on Fig. 1.[2] The new position of the center is $2\rlap{.}''6$ from the position given by Djorgovski & Meylan (1993b), which was the position used in targeting the central FOC field—thus explaining the near-miss of the center. The uncertainty in the position of the center is at least $0\rlap{.}''5$.

---

[2] This position corresponds to ($497, 310$) on the $V-$band PC image and ($50.4, 195.3$) on our $V-$band central FOC pointing (the upper half of Fig. 1). These two images are available from the HST Archive; their rootnames are U2AS0301T and X2L50201T, respectively.

3.2. The Surface-Density Profile

The surface-density profiles of stars in the inner $12''$ of M30 are shown in Figure 3, and are also given in Table 1. Points connected by lines in Fig. 3 refer to corrected counts, and lines without points refer to uncorrected (raw) counts. The stars are divided into three magnitude bins. The brightest bin (solid lines) contains stars in the range $18.75 < V < 20.25$ (corresponding to $0.76M_\odot > M > 0.69M_\odot$, according to BV92). The middle bin (dotted lines) contains stars with $20.25 < V < 21.75$ ($0.69M_\odot > M > 0.57M_\odot$), and the faintest bin (dashed lines) contains stars with $21.75 < V < 23.25$ ($0.57M_\odot > M > 0.49M_\odot$).

The density measured in each radial and magnitude bin was corrected for incompleteness using the matrix method of Drukier $et\ al.$ (1988, see Paper I)[3]. Points are plotted in Fig. 3 only when at least half of the artificial stars in the given bin were recovered; the middle magnitude range is thus usable only for $r > 2''$, and the faint range only outside of $3''$.

As expected, the density of stars in the brightest magnitude range rises going into the cluster center, with a power-law slope near -0.8. The density profile of the middle group is very similar. The profile of the faintest bin appears to have a somewhat flatter slope, although the errors are large enough for this last bin that its slope cannot be distinguished from the other two.

The innermost points of the brightest bin are consistent with either a continuation of the density cusp into the very center of the cluster, or with a small core of radius $< 2''$. In Paper I, we found that the small number of turnoff stars in the central $\sim 1''$ of M15 made it impossible to tell the difference between a cusp and a small core. With less than half the number of stars here, the distinction is even more difficult.

3.3. Maximum-Likelihood Profile Fitting

As in Paper I, we used a maximum-likelihood method to fit our star counts to parameterized density profiles of the form

$$f(r; \alpha, r_c) = \frac{1}{[1 + C_\alpha (r/r_c)^2]^{\alpha/2}}, \tag{1}$$

where α is the asymptotic logarithmic cusp slope (for $r \gg r_c$), and r_c is the core radius (the radius at which the projected density reaches half its central value; the constant $C_\alpha \equiv 2^{2/\alpha} - 1$ makes this so for any reasonable α).

Since the star counts are not complete, and the incompleteness varies with position in the image, the observed counts must be fit to a distribution that has incompleteness incorporated into

---

[3]As a check, we also tried correcting for incompleteness with a simpler method that ignored bin-jumping (i.e., we simply counted the fraction of artificial stars in a bin that were recovered, regardless of their output magnitude). The results were completely consistent with what is shown in Fig. 3.

it. (Fitting profiles to the corrected counts is not a good procedure, for reasons explained in Paper I.) So, the counts were actually fit to the product $g(r) = f(r)p_{\mathrm{m}}(r)$, where f is one of the functions defined above, and p_{m} is the probability that a star will be detected by our analysis procedure.

The profile fit requires values of p_{m} at the radius of each real star. We found these values from the database of artificial stars by the following procedure (which is explained in more detail in Paper I): We begin by considering the annular region defined by the 1250 artificial stars nearest in radius to the star in question. (Near the cluster center, this region is actually circular.) Within that region, we use the Drukier matrix method to correct the local observed LF for incompleteness. The ratio of the appropriate magnitude bins in the local observed and corrected LFs gives us the value of p_{m} at the radius in question. We then smooth p_{m} to remove noise that leads to problems in the fitting.

The completeness fraction p_{m} is shown in Figure 4 for each of the three magnitude ranges given in the previous section. (The remaining fluctuations in p_{m} are a result of insignificant local variations in density within the annulus in which p_{m} is computed; they do not affect the profile fit.) The brighter two magnitude bins are more than 90% complete over most of the field; the completeness of the brightest drops to $\sim 65\%$ in the central $2''$, while the second-brightest falls more quickly. The completeness of the faintest bin fluctuates between 60% and 80%. Along with the scatter in its binned density profile (Fig. 3), the larger fluctuations in this group's completeness indicate that there are simply too few stars in the group to measure its profile within the cusp with confidence.

In Figure 5, we show the likelihood function for the brightest group as a function of α and r_c. The point of maximum likelihood lies at $\alpha = 0.70$ and at small r_c. As in M15, models with core sizes up to $\gtrsim 1''$ fit nearly as well as the pure-cusp model; the 95% upper limit on r_c is $1''.9$. The 1-sigma uncertainty of α is 0.08, and its 95% confidence limits are ± 0.18.

In Figure 6, we show the likelihood functions for the brightest and the middle group, as a function of the cusp slope α only. The core radius r_c was held fixed at $1''$ for this computation, and stars within $1''.6$ of the center were not used, so that the same radial range could be used for both groups. Because of these small differences from the parameters used in making Fig. 5, the best-fit cusp slope for the brightest group is 0.76 ± 0.07 (1-sigma) in Fig. 6, vs. 0.70 in the previous case. The middle group's best-fit cusp slope is slightly steeper: 0.82 ± 0.11. Note that the cusp slopes of these two groups are consistent with each other.

3.4.   Comparison with the $r = 4'.6$ Field

Next, we look at the cluster cusp as a whole, with the goal of comparing its overall mass function (MF) with a MF measured farther out in the cluster.

The completeness-corrected luminosity function (LF) is shown in Figure 7, for two radial

ranges within the central cusp ($0'' < r < 6''$ and $6'' < r < 12''$). (These are the same data as are plotted in Fig. 3, but the star counts are now binned in magnitude within wider radial ranges, rather than the reverse.) The LFs are tabulated in Table 2. Next, we convert the magnitudes to masses, using the BV92 isochrone plotted in Fig. 2. The resulting MFs are plotted in Figure 8, along with the MF measured at $r = 4\rlap{.}'6$ (very close to the cluster half-mass radius) by Piotto, Cool, & King (1997), using the WFPC2. The MFs are also given in Table 3.

Note that the cusp LFs and MFs shown in Figs. 7 and 8 cannot be taken to represent the LF or MF at any single radius, since they are an average over the oddly-shaped observed area. Model predictions should be integrated over the same area in order to be compared with these data. To allow future modelers to do this integration, the corners of the observed area, relative to the cluster center, are given in Table 4.[4]

The two cusp MFs shown in Fig. 8 are very similar, except for the lower overall density farther out in the cusp. This observation reinforces the conclusion that the cusp slopes for the two mass groups presented in §3.3 are consistent with each other.

A comparison with the $r = 4\rlap{.}'6$ MF, on the other hand, shows strong mass segregation, in the sense expected from two-body relaxation, and also as expected from the observations of Bolte (1989). One way of making a direct and quantitative comparison of the three MFs is to fit a power law to each, over the range in mass where they overlap, and compare the power-law slopes. (Since the MFs are not well fit by power laws, this comparison is rather rough.) Over the range from 0.50 to 0.76 $M_\odot$, the best-fit slope for the $0'' < r < 6''$ MF is -3.1 ± 0.5; for the $6'' < r < 12''$ MF it is -3.8 ± 0.7, and for the $r = 4\rlap{.}'6$ MF it is 1.9 ± 0.6, where the Salpeter slope is 1.35. (The $r = 4\rlap{.}'6$ value is particularly sensitive to the choice of the low-mass cutoff in the fit. For this reason, its slope here differs from that given for M15 in Paper I, despite the fact that Piotto *et al.* [1997] found the two MFs to be indistinguishable.) Over the indicated mass range, then, the outermost MF differs from either of the inner two at the 6σ level. This comparison is crude, but confirms that the outer and inner MFs differ dramatically.

4.   King–Michie Modeling

As a first step towards modeling M30, we used our data to construct a King–Michie model of the cluster, as we did in the previous paper for M15. King–Michie models have a lowered-Maxwellian distribution function (Michie & Bodenheimer 1963, King 1966), which approximates the steady-state solution of the Fokker–Planck equation (King 1965). These models do not incorporate all of the important physical effects, most notably, the deviation from the lowered-Maxwellian DF late in core collapse (Cohn 1980). However, they are among the simplest models that can give a prediction of the variation of the MF from the center of the cluster to its

---

[4]The corners of the M15 fields from Paper I may be obtained from the author.

edge—in fact, a fairly realistic prediction, if their assumption of equipartition is correct (see the next section).

We used the Gunn & Griffin (1979) formulation of the multimass King–Michie model. We calculated the model by first choosing core and tidal (limiting) radii of 0.04 pc (= $1.''1$, at a distance of 7.5 kpc) and 28.5 pc (= $13.'2$), respectively, to agree with observation. (The value of r_c is somewhat arbitrary, but any value less than $2''$ leads to a nearly identical model.) Next, we defined sixteen mass groups, whose numbers of stars and average masses were constrained to agree with the MF observed by Piotto $et\ al.$ (1997) at $r = 4.'6$. (The measured densities were actually rounded off slightly, to make the plotted MFs more readable.) We then added a group of 0.55 $M_\odot$ white dwarfs, chosen (again, somewhat arbitrarily) to contain 20% of the cluster mass. Finally, we added 1.33 $M_\odot$ dark remnants (1.4% of the cluster by mass), whose number and mass were chosen to make the central density cusp agree with the observed surface-density profile. The model velocities are isotropic at all radii; since we found a good fit to the observed surface-density profile (SDP) with an isotropic model, we saw no reason to add velocity anisotropy.

A comparison of the model with observation is shown in Figure 9, and the model parameters are summarized in Table 5. The lower right and upper left panels of Fig. 9 show model quantities that were constrained to agree with observation; these panels confirm that the iteration procedure converged. The lower right panel shows the model MF at $r = 4.'6$, and the MF measured at that radius by Piotto $et\ al.$ (1997). The upper left panel shows the surface-brightness profile (SBP) of M30 given by Trager, King, & Djorgovski (1995), and the density profile of stars with $18.75 < V < 20.25$ from Fig. 3. The subpanel just below the upper left panel shows the logarithmic difference, on an expanded scale, between the SDP of group 1 of the model and the observed SBP.

The lower left and upper right panels show tests of the model, since the quantities plotted in those panels were not constrained to agree with observation. The lower left panel shows the velocity-dispersion profile (VDP) of the giants (the $0.78 M_\odot$ group). The solid jagged line is the VDP measured by Gebhardt $et\ al.$ (1995), who used a nonparametric method to turn their individual velocity measurements into a profile. The dashed lines above and below this line are the 90% confidence band on their VDP. The heavier, smooth line is the model-predicted VDP for the same stars. King–Michie models are isothermal in their center, so the model here does not reproduce the rise in velocity dispersion in the inner arcminute of M30.

The upper right panel shows the two FOC mass functions from Fig. 8, along with the MFs predicted by the model (which have been integrated over the actual observed field). Note that the agreement of the observed MFs with the model MFs at the high-mass end is a result of the fit of the surface-brightness profile, but the low-mass part of the MF was not constrained in any way. The model agrees with the observed MFs at the low-mass end quite well.

5. Discussion

For M30, our two main results are as follows: (1) Within the central cusp, there is very little mass segregation. (2) The overall MF of the cusp, though, is quite different from the MF at $4.'6$, and the difference is consistent with the predictions of a King–Michie (KM) model. In M15, on the other hand (Paper I), a comparison of the overall cusp MF with the outer MF revealed that their difference was smaller than a KM model would predict. Now, our next step is to determine what these mass-segregation measurements imply about the dynamical states of the two clusters.

This task is made more difficult by the fact that the KM models do not fit the Gebhardt *et al.* velocity-dispersion profiles. That lack of agreement implies that the KM models also do not have the correct cluster potentials and distribution functions (DFs); thus, we might not expect them to predict the correct degree of mass segregation, either (in which case our model comparisons would be meaningless). An alternative approach would be to run a set of computational simulations, such as Fokker–Planck or N-body models. Those evolving models, though, often have the ability to fit *too* easily, in the sense that decent fits can be found at one model time or another for many different sets of input parameters. In that case, it becomes difficult to determine which of the physical effects are most important.

Instead, here we will take a more direct approach, by trying to determine what our data imply about the current state of the cluster *without* assuming that the DF has any particular form, or that its present form must be the result of a specific set of physical processes. A number of recent globular-cluster studies have adopted a similar philosophy; see, for example, Merritt & Tremblay (1994), Cote *et al.* (1995), or Gebhardt & Fischer (1995).

What, then, can observations of mass segregation tell us about the structure of a cluster? Suppose that we somehow knew the form of the cluster potential, say, by inferring it from a large number of measurements of giant-star velocities. In a known potential, the observed degree of mass segregation reflects the allocation of energy between various stellar species, since groups of stars with lower (*i.e.*, more strongly bound) energies will tend to be found deeper in the potential well. The classical view is that a cluster should evolve towards equipartition of energy, in which two stellar species a and b would have velocity dispersions $\langle v_{\rm a}^2 \rangle$ and $\langle v_{\rm b}^2 \rangle$ such that $m_{\rm a}\langle v_{\rm a}^2 \rangle = m_{\rm b}\langle v_{\rm b}^2 \rangle$ at the cluster center.[5] However, core-collapse simulations have shown that equipartition is usually *not* achieved. In fact, as Spitzer (1969) first showed, the initial attempt to approach equipartition leads to a runaway contraction of the group of high-mass stars, and this "equipartition instability" leads to rapid core collapse in any cluster with a realistic mass function (Inagaki & Saslaw 1985).

---

[5]Actually, this condition is correct only for systems in which the DF is strictly Maxwellian. The lowering of the Gaussian in the King–Michie DF implies that KM models are not truly in equipartition (Pryor, Smith, & McClure 1986). A more general condition for equipartition is that the rate of exchange of kinetic energy between species is zero; for more details, see §8.3 of Binney & Tremaine (1987). However, high-concentration KM models do satisfy the simpler condition given above quite closely, near their centers.

Now, if a cluster *is* in equipartition, lower-mass stars will tend to have higher velocities at the center than higher-mass stars, so they will tend to reach larger radii, and will have a flatter density profile. On the other hand, if the species are not in equipartition, then the relative density distributions will differ from the equipartition prediction: for example, if one species has velocities that are "too high," its density profile will be flatter than it would be in equipartition. The current spatial distributions of stellar species thus reflect the ability of stellar encounters to transfer energy between species over the course of the cluster history, and give us a view not only of the present structure of a cluster, but also of its past.

Our present stumbling block, though, is our lack of knowledge of the cluster potential. However, we shall see below that having a *detailed* model of the potential is less important than it may initially seem.

5.1. The Cluster Envelopes

For the moment, let us consider the comparison of the central MFs with the outer MFs in each of the two clusters, and leave the mass segregation within the central cusps for later.

5.1.1. Mass Segregation as an Indicator of Equipartition

As described above, if the KM-model potentials had resulted in velocity-dispersion profiles that fit the observations, then the agreement (for M30) or disagreement (for M15) of the model-predicted mass segregation with observation would have directly indicated whether the relevant stellar species were in equipartition. Without a well-fitting model, we must find another way to infer what our observed densities imply about the stellar velocities.

Since the relaxation time at any radius in a globular cluster is much longer than the crossing time at that radius, we can approximate the cluster as being nearly collisionless. For our purposes here, let us also assume that each cluster has an isotropic velocity ellipsoid at all radii, and that neither of the clusters rotate. The density and velocity profiles should then obey the isotropic non-rotating Jeans equation, which in spherical coordinates is (see §4.2.1[d] of Binney & Tremaine 1987):

$$M(r) = -\frac{rv_j^2}{G}\left(\frac{d\ln\nu_j}{d\ln r} + \frac{d\ln v_j^2}{d\ln r}\right),\tag{2}$$

where $M(r)$ is the total mass enclosed within radius r, and ν_j and v_j^2 are the spatial density profile and the radial component of the velocity-dispersion profile, respectively, of species j. For two species j and k, the ratio of radial velocity dispersions at any radius must then be

$$\frac{v_j^2}{v_k^2} = \frac{(d\ln\nu_k/d\ln r) + (d\ln v_k^2/d\ln r)}{(d\ln\nu_j/d\ln r) + (d\ln v_j^2/d\ln r)}.\tag{3}$$

In principle, given the density profiles of two species and the VDP of one species j (say, the giants), Eq. 3 would allow us to solve for the unobserved VDP of the other species k (say, a group of lower-mass stars). Our interest here, though, is not in the VDP of the lower-mass stars itself (since we do not have enough information to determine it with much confidence), but in the value of the velocity ratio v_j^2/v_k^2 near the cluster center. If we can find a way to use the available data to infer this value, then we will know whether the species are in equipartition, *i.e.*, whether they satisfy the condition $m_j v_j^2 = m_k v_k^2$.

Below, we will describe how we used the observed densities (of both giants and lower-mass stars) and velocities (of giants) in each cluster to infer the velocity ratio given by Eq. 3. In the end, it will turn out that this procedure will confirm the impression given by the King–Michie models in the previous section: the data presented in this paper are consistent with M30 being in equipartition, while the data from the previous paper show that M15 is not. Before continuing the discussion of our method, it is worth asking why the KM models give nearly the right answer on the equipartition question, despite the fact that they fall short in other ways. The answer to this question will provide some insight into the relative importance of density and velocity measurements in constraining different aspects of cluster structure.

To see the reason for the KM models' success, note that the observed VDP slopes $(d \ln v^2/d \ln r)$ are much smaller than the density-profile slopes $(d \ln \nu/d \ln r)$ over most of each cluster's radial range. Now, consider a hypothetical set of cluster models that all have the same density profiles for species j and k. The VDPs (and thus the potential and distribution functions) may differ from model to model, but those differences change the value of the numerator and denominator of Eq. 3 by very little; thus, all models within the set must have nearly the same velocity ratio. In other words, while the VDP of one particular species may differ from model to model, the *ratio* of the VDPs of a pair of species *cannot* differ greatly between models.

To be more specific, imagine that we had a model of, say, M30, that used a non-King–Michie DF. Suppose further that this model was a correct and complete representation of the cluster structure, in the sense that it reproduced all of the available data: not only would it fit the density profiles of both the giants and the lower-mass stars (as did our KM model above), but also the VDP of the giants (whose slope was not fit by our KM model). Now, since this non-KM model and our KM model have identical density distributions for the giants and identical density distributions for the low-mass stars, they must be members of a set of the type defined above, and Eq. 3 then requires that the velocity ratios of the two models be similar. But, since our KM model is in equipartition, the non-KM model must then be close to equipartition as well—and, therefore, so must the cluster itself!

What we have shown (in an approximate way) is the following: If the observed *densities* in a cluster (such as M30) are well fit by the density distributions of a KM model fit to that cluster, then the cluster must be fairly close to being consistent with *all* predictions of some other non-KM model that is also in equipartition. Conversely, if a cluster is far from matching KM-model

mass-segregation predictions (e.g., M15), then *no* equipartition model can adequately describe the cluster, since all such models would make similar mass-segregation predictions (by an argument similar to the one given above). Thus, even though the KM DF was originally derived without a knowledge of many of the physical processes that actually take place in a cluster, KM-model *fitting* nevertheless remains a valuable part of cluster-structure studies, since the models make useful mass-segregation predictions, and are much easier to calculate than more sophisticated models.

Our approach here, then, will be to use our data to infer the run of the velocity ratio v_j^2/v_k^2 with r that pertains to each cluster, along with an estimate of its uncertainty. If this inferred run of the ratio is consistent with the run of the ratio from the KM model, and approaches m_k/m_j near the cluster center, then we may conclude that the stellar species are in equipartition, to within our measurement errors. On the other hand, if the run of v_j^2/v_k^2 found by the method is consistently and significantly larger (or smaller) than the run of v_j^2/v_k^2 of the cluster's KM model, then the lower-mass stars (species k) must have velocities that are lower (or higher) than the equipartition velocities.

5.1.2. Detailed Procedure

In practice, there are several difficulties that we must overcome if we wish to use Eq. 3 to find v_j^2/v_k^2 as a function of r: (1) We have the *projected* density profile of the giants, not the spatial profile. (2) For the lower-mass stars, we have even less information: only a few points on the projected profile. (3) We also see the VDP of the giants in projection, and it is noisy.

We can get around these difficulties, at least in part, using the following methods, which take advantage of the fact that we have already fit KM models to the clusters:

(1) **The densities of the giants.** For the spatial-density profile of the giants (group j), we use the giants' spatial-density profile from the KM model of the cluster in question. (Recall that the projection of this spatial profile was fit to the observed surface-brightness profile.) Although it is possible that the deprojection of the observed profile is nonunique, the possible range of the spatial profile should be small, since the profiles are always rather steep. (For a steep spatial profile, line-of-sight effects are less important than the profile slope in determining the shape of the projected profile.)

(2) **The densities of the lower-mass stars.** For the density profile of the group of lower-mass stars (group k), we choose a density profile from the KM model that fits the projected profile of that group at the observed radii. For M30, since the model-predicted mass segregation fits the observations, we simply use the actual KM-model profile for the lower-mass group k. For M15, we take a different profile l from the model: one whose radial ratio of projected density (Σ) between two of our M15 fields outside the cusp, $\Sigma_{l,\mathrm{model}}(20'')/\Sigma_{l,\mathrm{model}}(4.'6)$, matches the observed $\Sigma_{k,\mathrm{obs}}(20'')/\Sigma_{k,\mathrm{obs}}(4.'6)$ of group k.

Admittedly, this matching of the density ratio is a very crude way of "fitting" a profile to two density measurements. We have no way of knowing how well the radial derivative of the selected profile l matches the actual $d\ln\nu_k/d\ln r$ of the lower-mass group k, but without further observations, we have little choice.

(Note that this use of the model density profile does *not* imply that our results are dependent on the KM distribution function or potential. The model density profiles are used only as fitting functions, since King–Michie profiles are known to fit globular clusters well.)

(3) **The velocity-dispersion profiles.** Since the observed VDPs of the giants are noisy, we do not actually use them; in fact, we could not even evaluate Eq. 3 without deprojecting the observed VDP. Rather than attempting a deprojection, we take the following alternative approach: We solve Eq. 2 for the VDP of both the giants (v_j^2) and of the lower-mass stars (v_k^2), using a method to be described shortly, which will require us to assume a potential for the cluster. We then verify that the projected VDP of the giants that we have calculated is consistent with observation; if not, we adjust the potential and repeat the process until the projected VDP is adequate. The ratio of the calculated VDPs of the giants and of the lower-mass stars then gives a result equivalent to evaluating Eq. 3 directly.

The method used to solve Eq. 2 for $v^2(r)$ for each of the two mass groups, given an assumed $M(r)$ (equivalent to a potential), was as follows: For each group, we began by setting $d\ln v^2/d\ln r = 0$, and using Eq. 2 to solve for v^2 as a function of r. We then took a radial derivative of the computed v^2, and used that derivative as the $d\ln v^2/d\ln r$ term in Eq. 2 again. We then proceeded to alternate between computing v^2 and $d\ln v^2/d\ln r$ until both converged. The procedure did not converge in the central part of the cluster, where numerical inaccuracies in the density-profile derivative were amplified by the iteration procedure. Over most of its radial range, though, v^2 converged after a few iterations for both mass groups. We could then take the ratio of v^2 for the two groups, to get the desired velocity ratio.

In the first step of this procedure, we had to assume a potential. For reasons given earlier, the final velocity ratio is only weakly dependent on the exact form of the assumed potential; the only important constraint is that the projected VDP be consistent with the observed velocities of giants. Thus, we chose to assume as simple a form for $M(r)$ as was necessary to generate VDPs that were consistent with the Gebhardt *et al.* measurements: a power law. The only parameters in the $M(r)$ fit were the power-law exponent itself (which always corresponded to potentials that were steeper than an isothermal sphere), and the total mass within the cluster limiting radius. We found the appropriate values of the parameters by trial and error: we simply tried different parameter combinations until the projected VDP of the giants agreed with the Gebhardt *et al.* observations.[6]

---

[6]Note that all of our knowledge of the potential comes from the Gebhardt *et al.* data; our mass-segregation measurements give us no new information about either the potential or the form of the distribution function.

5.1.3. Results

The results of using this Jeans-equation procedure on the M15 and M30 data are shown in Figure 10.

The lower panel on each side of Fig. 10 shows the line-of-sight velocity dispersions of giants obtained by iteratively solving Eq. 2, as well as the Gebhardt *et al.* VDPs for each cluster. For M15, we used a potential $\propto r^{-0.2}$, taking the power law from the result of the nonparametric analysis of M15 velocity data by Gebhardt *et al.* (1997). For M30, we found a good fit to the velocities with a potential proportional to $r^{-0.6}$.

The solid lines in the upper panels of Fig. 10 show the ratio $v_{\text{giants}}^2/v_{\text{low-mass}}^2$ for both clusters, as calculated using Eqs. 2 and 3. For M30, the "low-mass stars" are a group with masses near $0.61 M_\odot$. For M15, the low-mass stars have masses near $0.52 M_\odot$, but in the iteration procedure we used a density profile for $0.62 M_\odot$ stars from the Paper I KM model, as discussed above. (Also, for M15 we used an isotropic KM model, rather than the anisotropic model given in Paper I, since our method here requires the assumption of velocity isotropy. The isotropic and anisotropic models make virtually identical mass-segregation predictions.)

The several solid lines shown in the upper panels of Fig. 10 are the velocity ratios found after various numbers of iterations (from 2 to 5). The curves separate from each other in the central cusp, where the solutions have not converged, but are quite consistent for $r > 10''$.

The dashed lines in each upper panel show the velocity ratio (for the same pair of species) predicted by the KM model of each cluster. Since the KM model is (nearly) in equipartition, the dashed line approaches the mass ratio $m_{\text{low-mass}}/m_{\text{giants}}$ near each cluster center. At larger radii, the KM-model velocity ratio approaches 1, as the tidal cutoff becomes more and more important.

For both clusters, the velocity-ratio curves found from the Jeans equation lie above the KM-model curve, implying that the low-mass stars have slightly lower velocities than they would if the two species were in equipartition (*i.e.*, the two species have velocity dispersions that are closer together than they would be in equipartition).

(Note that any other mass group could have been taken to represent the lower-mass stars in each cluster, with similar results. The exact values of $v_{\text{giants}}^2/v_{\text{low-mass}}^2$ would have been different, of course, but the solid curves lie above the dashed curves no matter which low-mass group is used.)

In interpreting Fig. 10, it is important to realize that we have inferred the run of the velocity ratio from a *small* number of measurements of the densities of low-mass stars in each cluster, not from a measurement of their entire density profile. Since we used KM-model density profiles as fitting functions in the iteration procedure, it should come as no surprise that our inferred velocity-ratio runs resemble those of the KM model as well, except that they are shifted in the vertical direction. The proper way to interpret each of the upper panels, then, is not to pay

attention to the details of the radial variation of $v^2_{\text{giants}}/v^2_{\text{low-mass}}$, but instead to regard each group of solid curves as a *single* measurement of their offset from the KM-model curve.

The crucial question, then, is whether those offsets are significantly different from zero. The two major sources of uncertainty in our Jeans-equation procedure are the errors in the MFs themselves, and our lack of detailed knowledge of the radial dependence of the potential. For both clusters, an estimate of the errors shows that the MF error dominates, and leads to an uncertainty of ~ 0.06 in $v^2_{\text{giants}}/v^2_{\text{low-mass}}$ at the innermost value of r for which the several curves plotted in each upper panel remain together before separating in the central cusps.

Within this formal error of 0.06, the M30 Jeans-equation curve is consistent with the KM-model curve for that cluster, while for M15, the Jeans-equation curve is $\sim 2.5\sigma$ away from the KM model. We conclude, then, that over our observed ranges in mass and radius in each cluster, the stellar species in M30 are in a state of equipartition of energy, while those in M15 most likely are not.

There are some potential sources of systematic error that we have neglected in this analysis. The most important of these is the possibility of velocity anisotropy in either of our clusters. An anisotropic velocity ellipsoid would lead to the presence of a third term on the RHS of Eq. 2. In that case, it would be more appropriate to determine the radial run of the ratio of $(v^2_{\text{r}} + 2v^2_{\text{t}})$, rather than the ratio of just v^2_{r}. We will not pursue such a computation here, but will merely note that strong anisotropy could seriously undermine our equipartition conclusions, particularly if the degree of anisotropy varied with radius, or especially if it differed for different stellar species.

This last possibility may not be so far-fetched. Takahashi (1996, 1997) and Takahashi *et al.* (1997) have investigated the development of anisotropy in Fokker–Planck models of multimass clusters, and have found that the degree of anisotropy can differ widely from model to model, and from species to species within a single model. Since there is no observational data that could constrain the shape of the velocity ellipsoid in either cluster, we can only consider the isotropic case, and leave the possibility of anisotropy as an open question. (The last of the three Takahashi papers finds that the velocity ellipsoid becomes more isotropic after core collapse, so for these two clusters, our assumption of isotropy may be fairly close to the truth.)

Our assumption of non-rotation might also be questioned, at least in the case of M15, where Gebhardt *et al.* (1997) have detected a small degree of rotation.

5.2. The Cluster Cusps

In principle, the same sort of Jeans-equation analysis could be applied to the data in the central $\sim 10''$ of all three clusters. However, the small number of stellar velocities measured in the cusps does not allow us to constrain the potentials well; in fact, it is not known with certainty whether any clusters harbor central massive objects. However, we *can* make some reasonable

assumptions about the potential, and ask what our data would then imply.

First, though, we compare the data with some simple models from the literature that take equipartition, rather than a particular potential, as a basic assumption.

5.2.1. Simple Equipartition Models

Post-core-collapse and black-hole models of cluster cusps in equipartition predict very different variations of cusp slope with mass, since the two models have greatly differing distribution functions. In a simple equipartition core-collapse model (Cohn 1980), the potential is proportional to $r^{-0.23}$, and there is a strong degree of mass segregation within the cusp, which can be described as follows: if $-\beta$ is the logarithmic slope of the spatial density cusp for a group of stars with mass m (with the projected cusp having slope $\alpha = \beta - 1$, for $\beta > 1$), then $\beta = 1.89(m/m_{max}) + 0.35$, where m_{max} is the mass of the stars that dominate the cusp (Cohn 1985). Black-hole cusps, on the other hand, have much weaker segregation (Bahcall & Wolf 1976, 1977); the potential is Keplerian (r^{-1}), and all of the stellar species have spatial cusp slopes between -1.75 and -1.50.

More specifically, then, in M30 the core-collapse model would require the presence of dark stellar remnants with masses of $\sim 1 M_{\odot}$ to account for the turnoff stars' projected slope of -0.76. This model would then predict a projected slope of -0.54 for the "middle" ($0.57 M_{\odot}$ to $0.69 M_{\odot}$) group in that cluster—a value 2.5σ away from the measured slope of that group (-0.82). It has also been suggested that an isothermal sphere in equipartition would be a good model of a cusp well after core collapse. Such a model, though, would also predict a projected slope near -0.5 for the lower-mass stars, and would not match the data.

The similarity of the two cusp slopes in M30 *is* quite consistent with the predictions of the black-hole model. However, kinematic evidence for a black hole in M30 is lacking. A black hole would induce a cusp in the velocity dispersion of giants, but Zaggia *et al.* (1992, 1993) concluded that the cluster is isothermal near its center, with $\langle v_{giants}^2 \rangle = 6.0$ km s^{-1}. The VDP estimated nonparametrically by Gebhardt *et al.* (1995; see Fig. 9) does rise in the center ($v_{giants}^2 \propto r^{-0.4}$), but more slowly than Keplerian. A Keplerian $v^2 \propto r^{-1}$ cusp would barely fit within their 90% confidence band, while an isothermal region like that found by Zaggia *et al.* would fit easily. Velocities have been measured for only a few cusp stars, though, and it is *possible* that a velocity cusp has been missed. A $\sim 1000 M_{\odot}$ black hole might be detected in a globular cluster by the STIS spectrograph recently installed on *HST*.

5.2.2. Non-Equipartition Models

An alternative to comparing our cusp slopes with models from the literature would be to use the procedure from §5.1 once again, this time using the observed cusp slopes to get values for

$d \ln \nu / d \ln r$. One step in the procedure was to find a potential that fit the observed velocities of giants; but with so few velocities for cusp stars, we have no hope of constraining the cusp potential in this way.

Instead, we can simply assume the same crude power-law potential that we fit to each cluster in §5.1. The density profile follows a power law within the cusp; if we assume that the velocity-dispersion profile $v_{\rm r}(r)$ and potential $\Phi(r)$ also follow power laws, then the Poisson equation requires that $d \ln v_{\rm r}^2 / d \ln r = d \ln \Phi / d \ln r$. Thus, the process of finding the velocity ratio $v_{\rm giants}^2 / v_{\rm low-mass}^2$ within the cusp becomes a simple matter of substituting the appropriate values into Eq. 3, rather than iteratively solving Eq. 2 as we did previously.

For M15, this Jeans-equation procedure is especially attractive, since the potential that best fit the Gebhardt *et al.* data was proportional to $r^{-0.2}$, and thus closely resembles the cusp potential predicted by Fokker–Planck core-collapse models. If we use this potential and our observed cusp slopes for the "turnoff" and "middle" groups from Paper I (-0.64 and -0.56, respectively) in Eq. 3, we find a value of 0.96 ± 0.09 for the ratio of squared central velocity dispersions for these groups of ~ 0.8 and $0.7 M_\odot$ stars. (Note that these are not the same groups that were used on the right side of Fig. 10.)

In equipartition, the value of the velocity ratio for these two M15 groups would be ~ 0.87. Our star counts therefore do not indicate a *significant* departure from equipartition in the cusp of M15, although we do not go deep enough that this measurement is very sensitive.[7] It is worth noting that since the publication of Paper I, Dull *et al.* (1997) have published a new Fokker–Planck model of M15, which matches our observed cusp slopes fairly well.

In M30, we can use the cusp slopes given in §3.3 for the "turnoff" and "middle" groups to find a velocity ratio of 1.03 ± 0.08 (assuming a potential proportional to $r^{-0.6}$, as we did in §5.1). The equipartition prediction for this ratio is 0.86, so our measurement is off by 2.1σ from this prediction.

Although our measurements do not entirely exclude the possibility of equipartition in either cusp, the similarity of the two measured slopes in each cluster is nevertheless quite intriguing. The density profile of each species within the cusp is a result of the behavior of the distribution function of that species at the lowest (*i.e.*, most strongly bound) energies. The observation that the cusp slopes are similar therefore suggests that those portions of the distribution functions are also quite similar, no matter what the potential might be within the cusp, and regardless of whether a black hole is present. However, the distribution functions of the various species cannot

---

[7]In Paper I, we showed that the M15 cusp star counts were not well matched by one particular equipartition core-collapse model, while here, we cannot say whether the cusp is in equipartition. The reason for the difference in conclusions is that the uncertainty of the velocity ratio given here includes a contribution from the uncertainty in the potential, which in turn arises from the uncertainty in the velocity-dispersion profile. The comparison in the previous paper, on the other hand, did not involve any velocity data—it was a comparison of density slopes only.

be *entirely* the same, since the MFs do vary with radius outside of the cusp. Thus, we are left with the possibility that the physical processes that govern the dynamics of the most strongly bound stars of the cluster—and that therefore determine the structure of the density cusp—may not be the same as the processes that determine the structure of the rest of the cluster. In the next section, we give some more speculative ideas for what might be happening in the cusps.

5.3.   An Evolutionary Scenario

Our main conclusions are as follows: (1) There are notable differences between clusters in the allocation of energy between stellar species, with some clusters, such as M30, being closer to equipartition of energy than others, such as M15. (2) In some cases, the cusp may be a different environment from the rest of the cluster, in the sense that there is less mass segregation within the cusp than one would expect from measurements outside of the cusp.

Let us consider the second conclusion first. A high binary fraction in the cusp, or the presence of a central black hole, would lead to a difference between the cusp and the envelope, or could account for differences between cusps of different clusters. Direct evidence for these circumstances is lacking, but either is plausible.

Even in a cluster composed only of single objects of stellar size, though, a concentrated population of heavy dark objects could account for these results, if we allow for dynamical evolution. Suppose that a cluster begins with similar density and velocity distributions for all stellar species, as a result of violent relaxation. The highest-mass stellar group will then undergo core collapse, as a result of the Spitzer equipartition instability. After core collapse, the central density of this highest-mass group is much higher than that of the present-day main-sequence stars, and the relaxation time of the subsystem of high-mass objects in the core and cusp is considerably less than the relaxation time in the surrounding envelope. The core and cusp might thus undergo rapid gravothermal oscillations, confined to the central few arcseconds, and the (relatively) few luminous stars in the cusp would simply react to the fluctuating potential produced as a result of these oscillations. What we observe in the cusp might then differ considerably, depending on the phase of oscillation in which we happen to see it.

After the first core collapse, what happens to the stars that spend most of their time in the cluster envelope? Energy production from binaries in the core has stabilized the cluster against further collapse, and compared to internal relaxation, external effects on the global MF operate rather slowly (unless the cluster suffers frequent tidal shocks). It is plausible that the stellar envelope can then continue its dynamical evolution towards equipartition, on timescales determined more by the overall properties of the cluster than by the properties of the core.

We might expect, then, that the stars in a cluster would reach equipartition at a given radius only when the cluster age becomes equal to the relaxation time at that radius. We can use our KM models of M15 and M30 to evaluate the relaxation time for each cluster at $r = 4\rlap{.}'6$, the radius

of our outermost observations: for M30, $t_{\rm r} \simeq 10$ Gyr, while for M15, $t_{\rm r} \simeq 40$ Gyr.[8] So, the $r = 4\rlap{.}'6$ field in M15 is at a radius where $t_{\rm r}$ is greater than the cluster age, while relaxation at $r = 4\rlap{.}'6$ in M30 should be nearly complete—a scenario that is entirely consistent with our observation that M30 is closer to equipartition than its more massive cousin.

It is plausible, then, that that the data presented here and in the previous paper represent two stages of the dynamical evolution of a typical old and dense globular cluster. Future observations of cluster MFs, in a variety of clusters and in a number of fields within each cluster, will tell us whether this scenario is close to the truth.

---

[8]In this computation we have taken the mean density inside of $r = 4\rlap{.}'6$ as the density of the stars being encountered, the overall mean stellar mass as the mean mass of the stars being encountered, and the velocity dispersion at $r = 4\rlap{.}'6$ as the velocity of the star suffering encounters. These quantities could be chosen somewhat differently, since the relaxation time is only an order-of-magnitude quantity, but the relaxation time for M15 would be considerably longer no matter how we do the computation.

REFERENCES

Bahcall, J. N., & Wolf, R. A. 1976, ApJ, 209, 214

Bahcall, J. N., & Wolf, R. A. 1977, ApJ, 216, 883

Bergbusch, P. A., & VandenBerg, D. A. 1992, ApJS, 81, 163 (BV92)

Binney, J., & Tremaine, S. 1987, Galactic Dynamics (Princeton: Princeton University Press)

Bolte, M. 1987, ApJ, 319, 760

Bolte, M. 1989, ApJ, 341, 168

Cohn, H. 1980, ApJ, 242, 765

Cohn, H. 1985, in Dynamics of Star Clusters, eds. J. Goodman & P. Hut, p. 161

Cote, P., Welch, D. L., Fischer, P., & Gebhardt, K. 1995, ApJ, 454, 788

Djorgovski, S. 1993, in Structure and Dynamics of Globular Clusters, ASP Conf. Ser. Vol. 50, eds. S. Djorgovski & G. Meylan (San Francisco: ASP), p. 373

Djorgovski, S., & King, I. R. 1986, ApJ, 305, L61

Djorgovski, S. & Meylan, G. 1993a, eds., Structure and Dynamics of Globular Clusters, ASP Conf. Ser. Vol. 50 (San Francisco: ASP)

Djorgovski, S., & Meylan, G. 1993b, in Structure and Dynamics of Globular Clusters, ASP Conf. Ser. Vol. 50, eds. S. Djorgovski & G. Meylan (San Francisco: ASP), p. 325

Drukier, G. A., Fahlman, G. G., Richer, H. B., & VandenBerg, D. A. 1988, AJ, 95, 1415

Dull, J. *et al.* 1997, ApJ, 481, 267

Gebhardt, K., & Fischer, P. 1995, AJ, 109, 209

Gebhardt, K., Pryor, C., Williams, T. B., & Hesser, J. E. 1994, AJ, 107, 2067

Gebhardt, K., Pryor, C., Williams, T. B., & Hesser, J. E. 1995, AJ, 110, 1699

Gebhardt, K., Pryor, C., Williams, T. B., Hesser, J. E., & Stetson, P. B. 1997, AJ, 113, 1026

Gunn, J. E., & Griffin, R. E. 1979, AJ, 84, 752

Hut, P. & Makino, J. 1996, eds., Dynamical Evolution of Star Clusters: Confrontation of Theory and Observations, IAU Symp. 174 (Dordrecht: Kluwer)

Inagaki, S. & Saslaw, W. C. 1985, ApJ, 292, 339

King, I. R. 1965, AJ, 70, 376

King, I. R. 1966, AJ, 71, 64

King, I. R., Anderson, J., & Sosin, C. 1994b, in Calibrating Hubble Space Telescope: Proceedings of a Workshop Held at STScI, eds. J.C. Blades & S.J. Osmer (Baltimore: STScI), p. 130

King, I. R., Sosin, C., & Cool, A. M. 1995, ApJ, 452, L33

Lugger, P. M., Cohn, H., & Grindlay, J. E. 1995, ApJ, 439, 191

Makino, J. 1996, in Dynamical Evolution of Star Clusters: Confrontation of Theory and Observations (IAU Symp. 174), eds. P. Hut & J. Makino (Dordrecht: Kluwer), p. 151.

Merritt, D., & Tremblay, B. 1994, AJ, 108, 514

Michie, R. W., & Bodenheimer, P. 1963, MNRAS, 126, 269

Piotto, G., Cool, A. M., & King, I. R. 1997, AJ, 113, 1345

Pryor, C., Smith, G. H., & McClure, R. D. 1986, AJ, 81, 546

Rubenstein, E. P., & Bailyn, C. D. 1997, ApJ, 474, 701

Sosin, C. & King, I. R. 1997, AJ, 113, 1328 (Paper I)

Spitzer, L. 1969, ApJ, 158, L139

Stetson, P. 1987, PASP, 99, 191

Stetson, P. 1992, in Astronomical Data Analysis Software, ed. D. M. Worrall, C. Biemesderfer, and J. Barnes (ASP Conference Series, Vol. 25), p. 297

Trager, S. C., King, I. R., & Djorgovski, S. 1995, AJ, 109, 218

Yanny, B., Guhathakurta, P., Schneider, D. P., & Bahcall, J. N. 1994, ApJ, 435, L59

Zaggia, S., Capaccioli, M., Piotto, G., & Stiavelli, M. 1992, A&A, 258, 302

Zaggia, S., Capaccioli, M., & Piotto, G. 1993, A&A, 278, 415
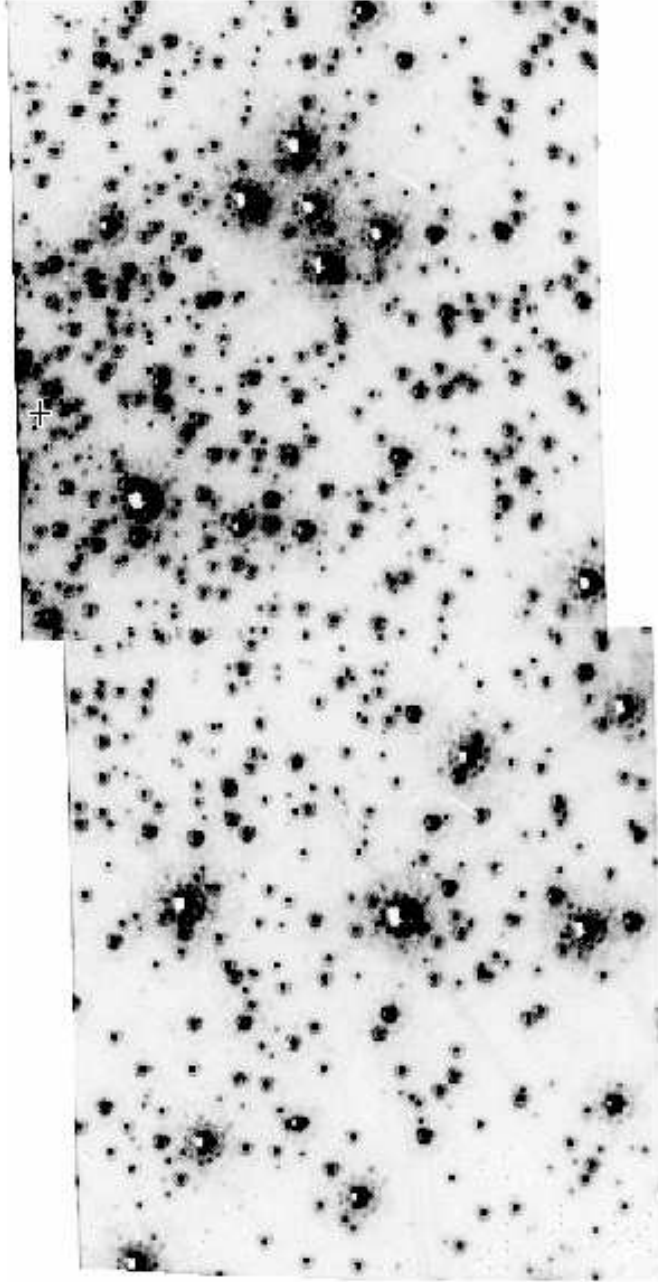
Figure 1.   F480LP (FOC "V") image of the two $7'' \times 7''$ FOC pointings in M30. The cluster center is indicated by a cross near the left edge of the upper pointing.
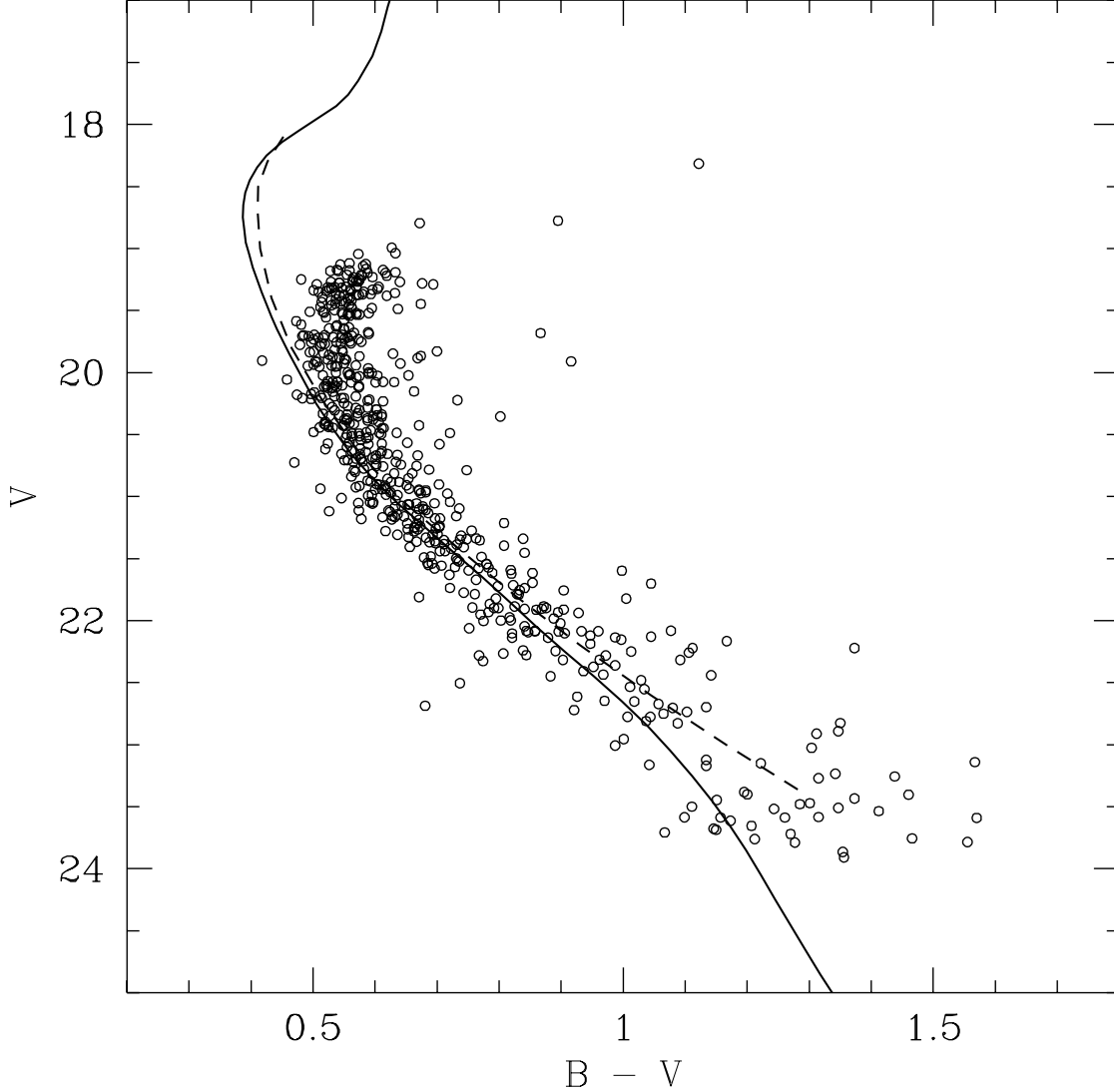
Figure 2. A color–magnitude diagram, in Johnson B and V, of the two FOC fields in M30. The dashed line is the main-sequence ridge line of Bolte (1987), and the solid line is the ([Fe/H] $= -2.03$, $t = 16$ Gyr) isochrone of Bergbusch & VandenBerg (1992). The redward deviation of the FOC points from the line is due to the onset of nonlinearity, which affects the B magnitudes more strongly than the V magnitudes.
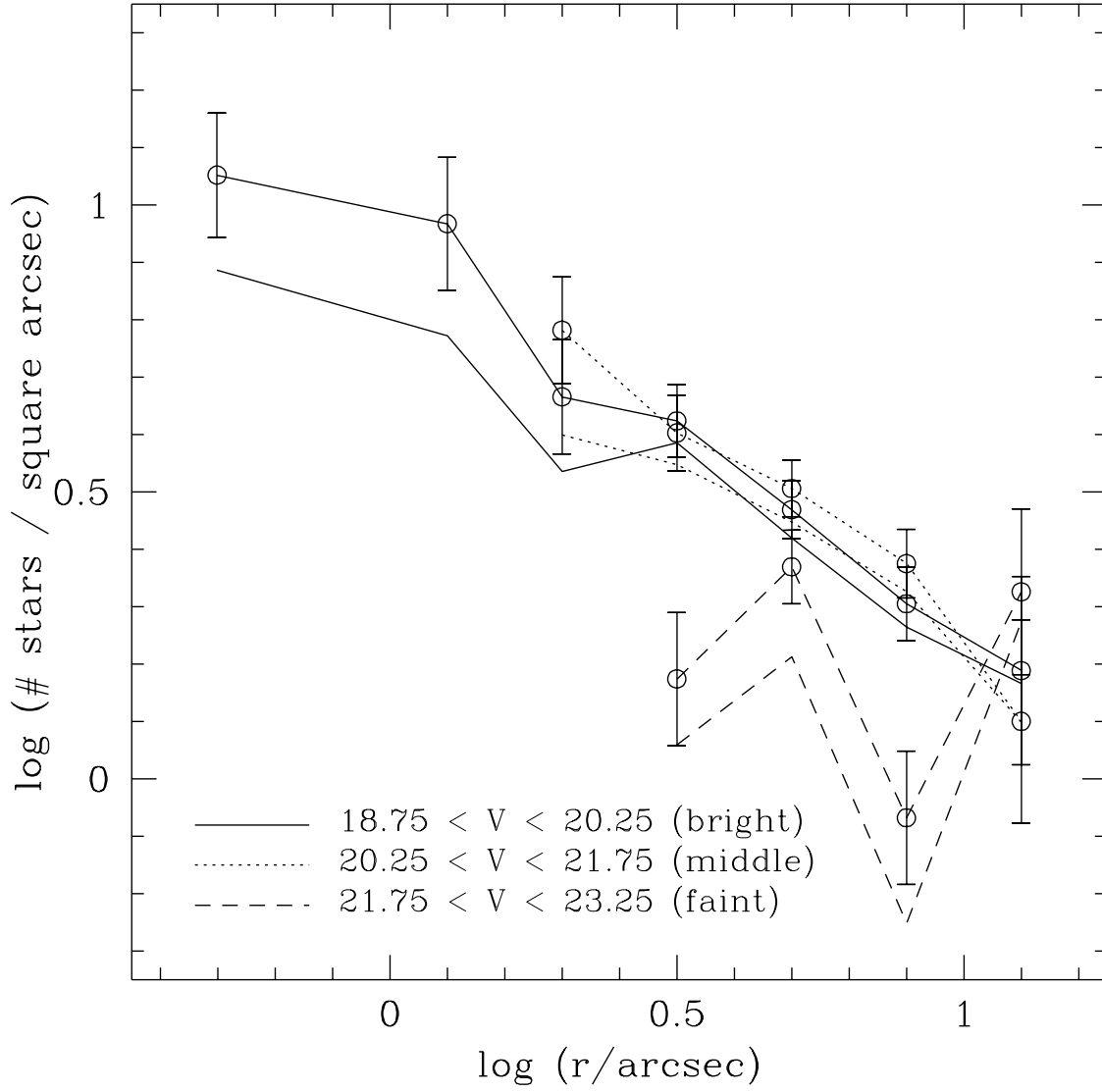
Figure 3. The projected stellar density in the cusp of M30, plotted in radial bins, in three magnitude ranges. The circular points connected by lines refer to the counts corrected for incompleteness. The lines without points show the "raw" (incomplete) counts.
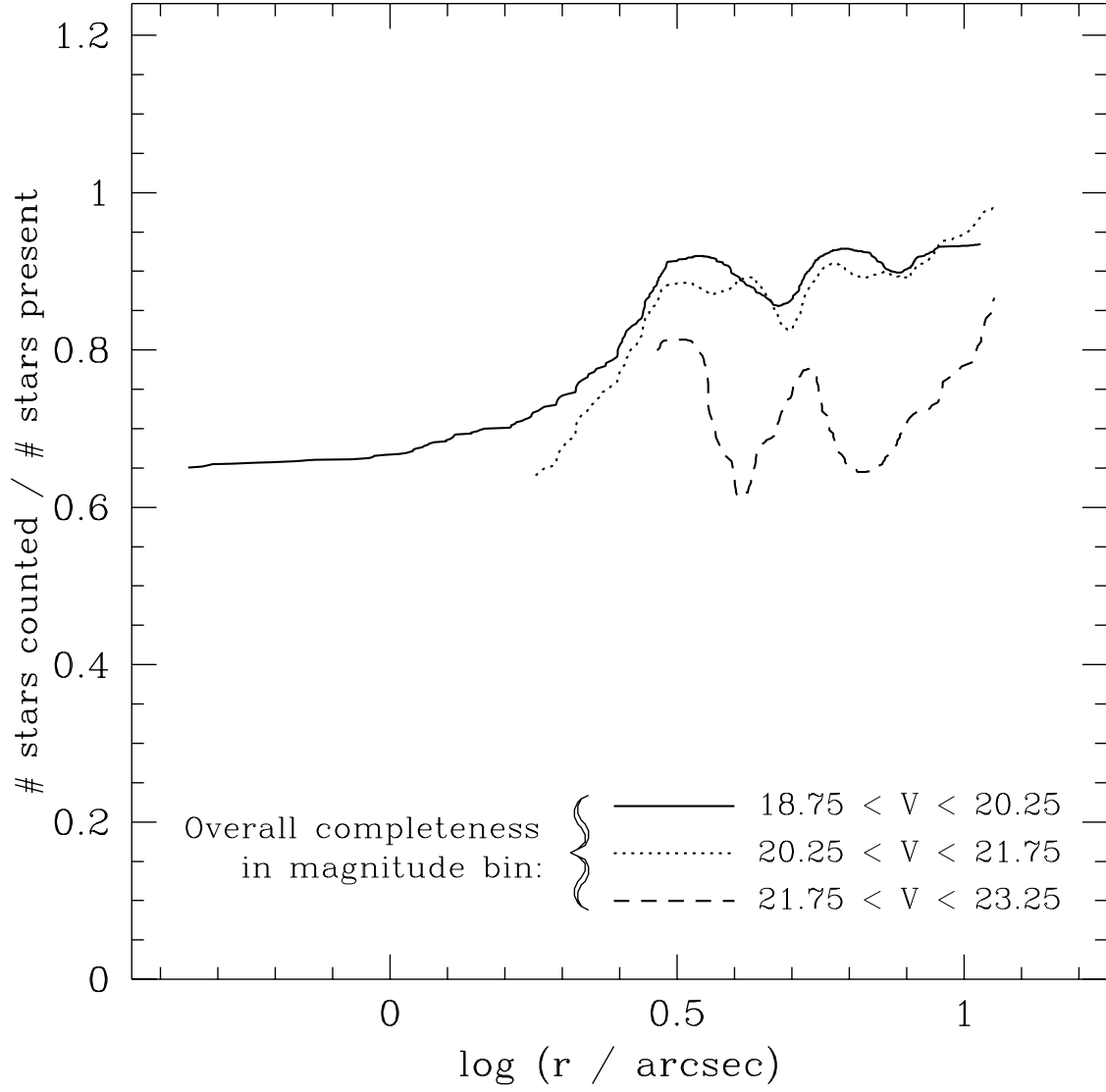
Figure 4. The completeness ratio $p_m(r)$ for the three stellar samples in M30. See the text for an explanation of the fluctuations.
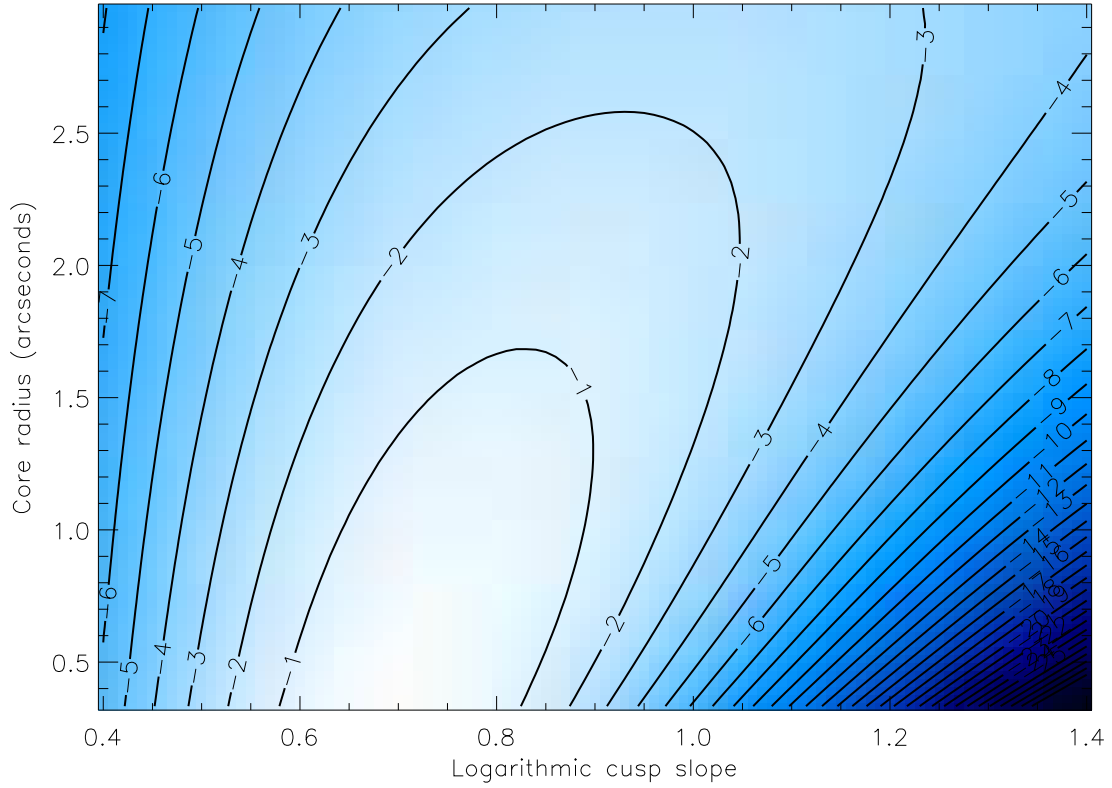
Figure 5. The log-likelihood of the "bright" M30 sample ($18.75 < V < 20.25$), as a function of the (negative) cusp slope α and core radius r_c in arcseconds, using the fitting function defined by Eq. 1. Lighter areas indicate a higher probability of seeing the observed counts. Contour lines are plotted one unit apart, so that each line represents a factor of 10 in the likelihood function. Thus, a model with an (α, r_c) pair that lies on the -2 contour line is one-tenth as likely to produce the observed counts as a model whose (α, r_c) lies on the -1 line. The point of maximum likelihood lies at $\alpha = 0.7$ and very small r_c.
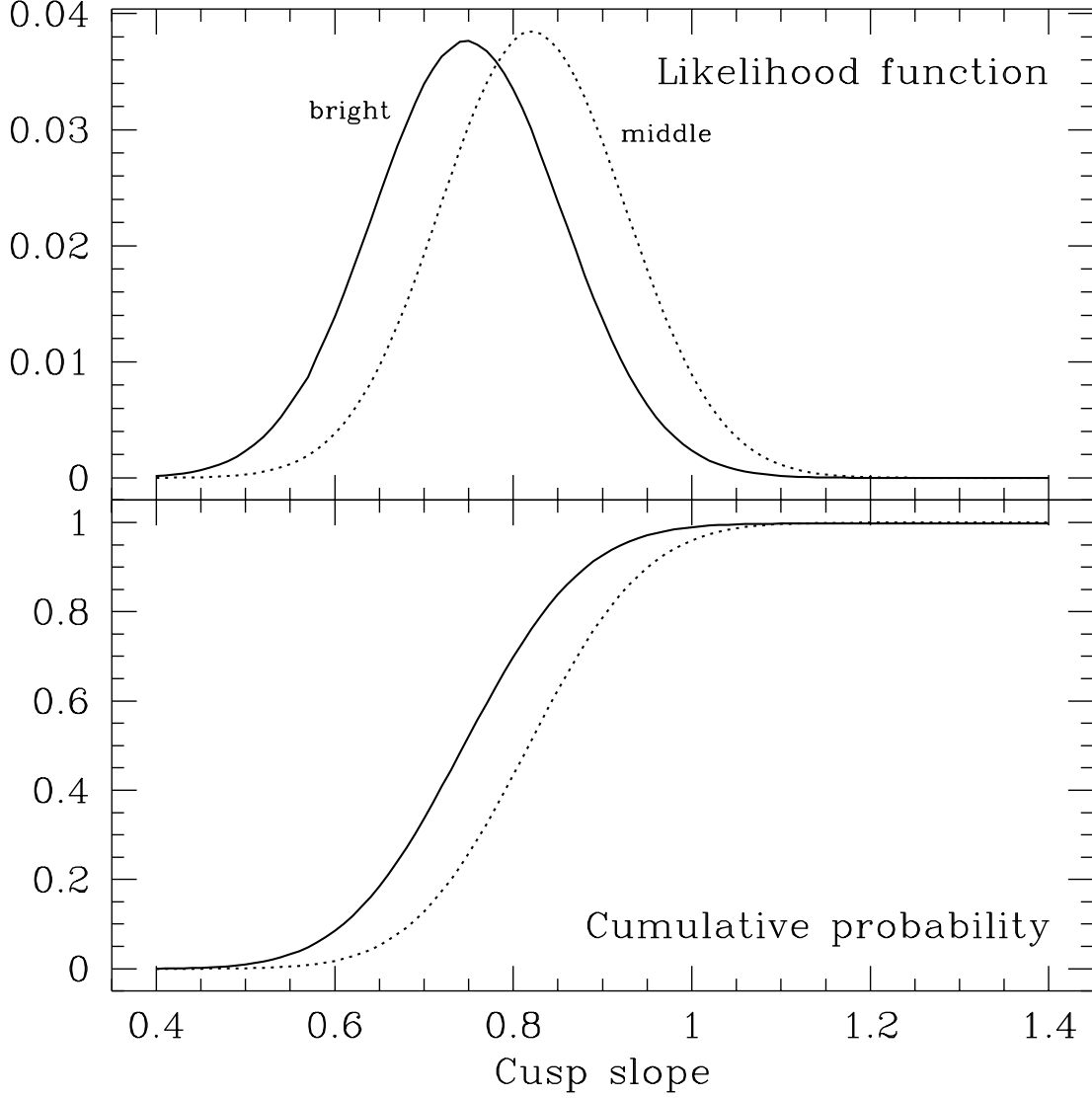
Figure 6. (Upper panel) The likelihood of seeing the observed M30 star counts as a function of the (negative) cusp slope α, for the brighter two stellar samples, using the fitting function defined by Eq. 1. The solid curve refers to the brightest magnitude bin ($18.75 < V < 20.25$), and the dotted curve to the middle bin ($20.25 < V < 21.75$) (Lower panel) The same likelihood functions converted to a cumulative probability, assuming a uniform prior.
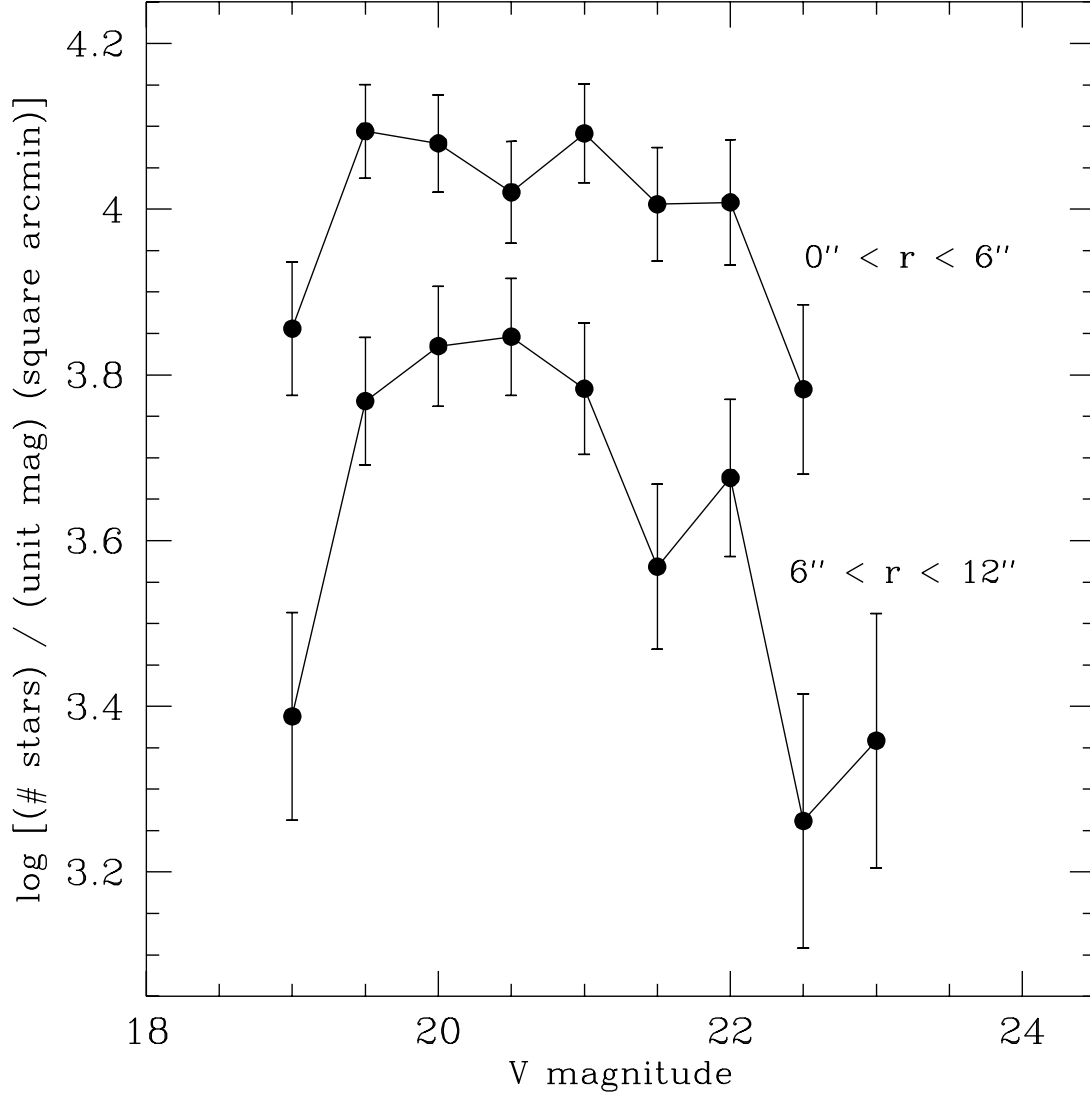
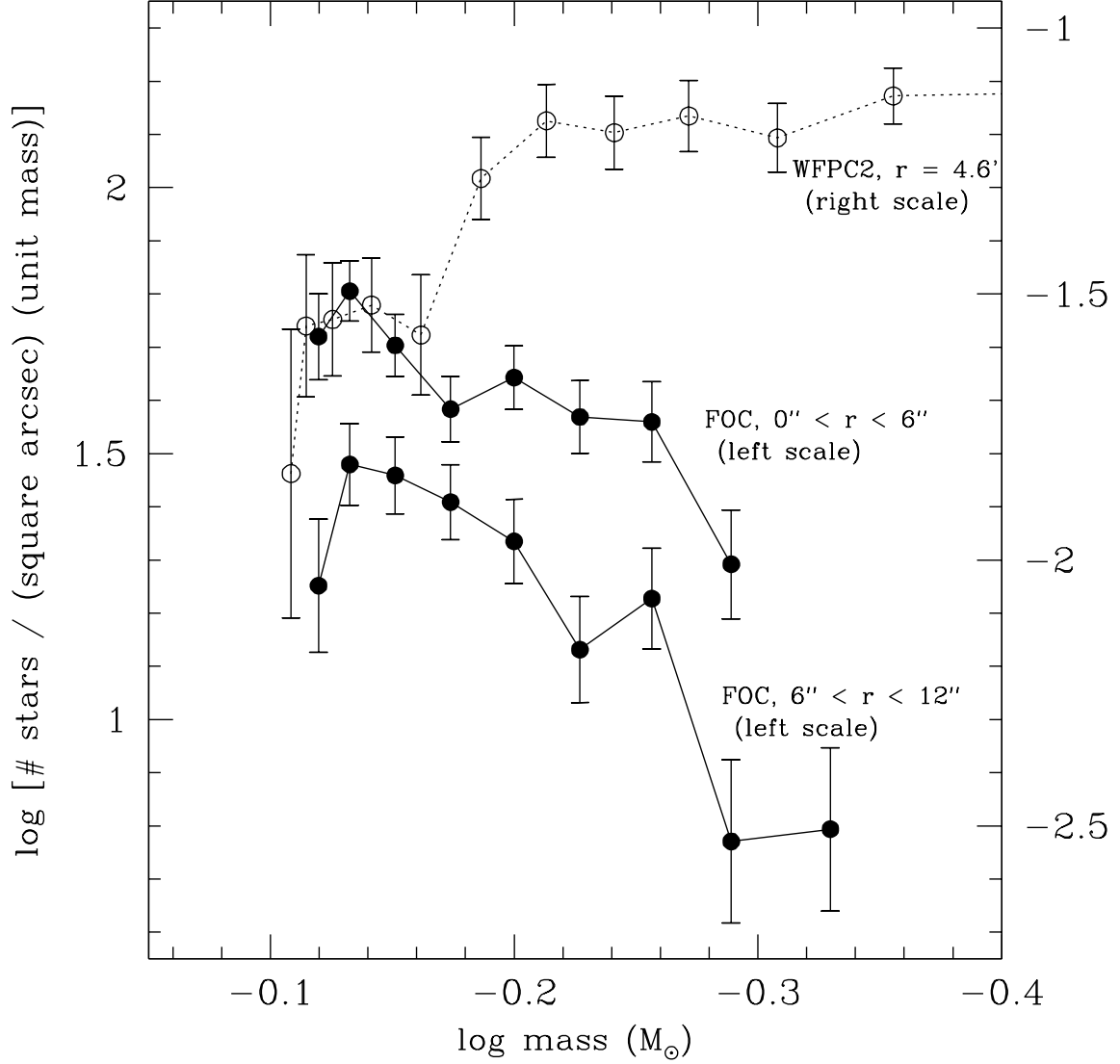Figure 7.   Luminosity functions in two radial ranges in M30.

Figure 8. Mass functions in two radial ranges in M30 (from our FOC images), and a mass function farther out in the cluster (from the WFPC2 images of Piotto, Cool, & King 1997). The two FOC MFs refer to the left-hand scale, and the outer WFPC2 MF refers to the right-hand scale. Since the stellar density is much lower in the $r = 4.6$ field, the vertical position of the WFPC2 MF has been chosen to match one of the FOC MFs at the bright end, so that the two may be easily compared.
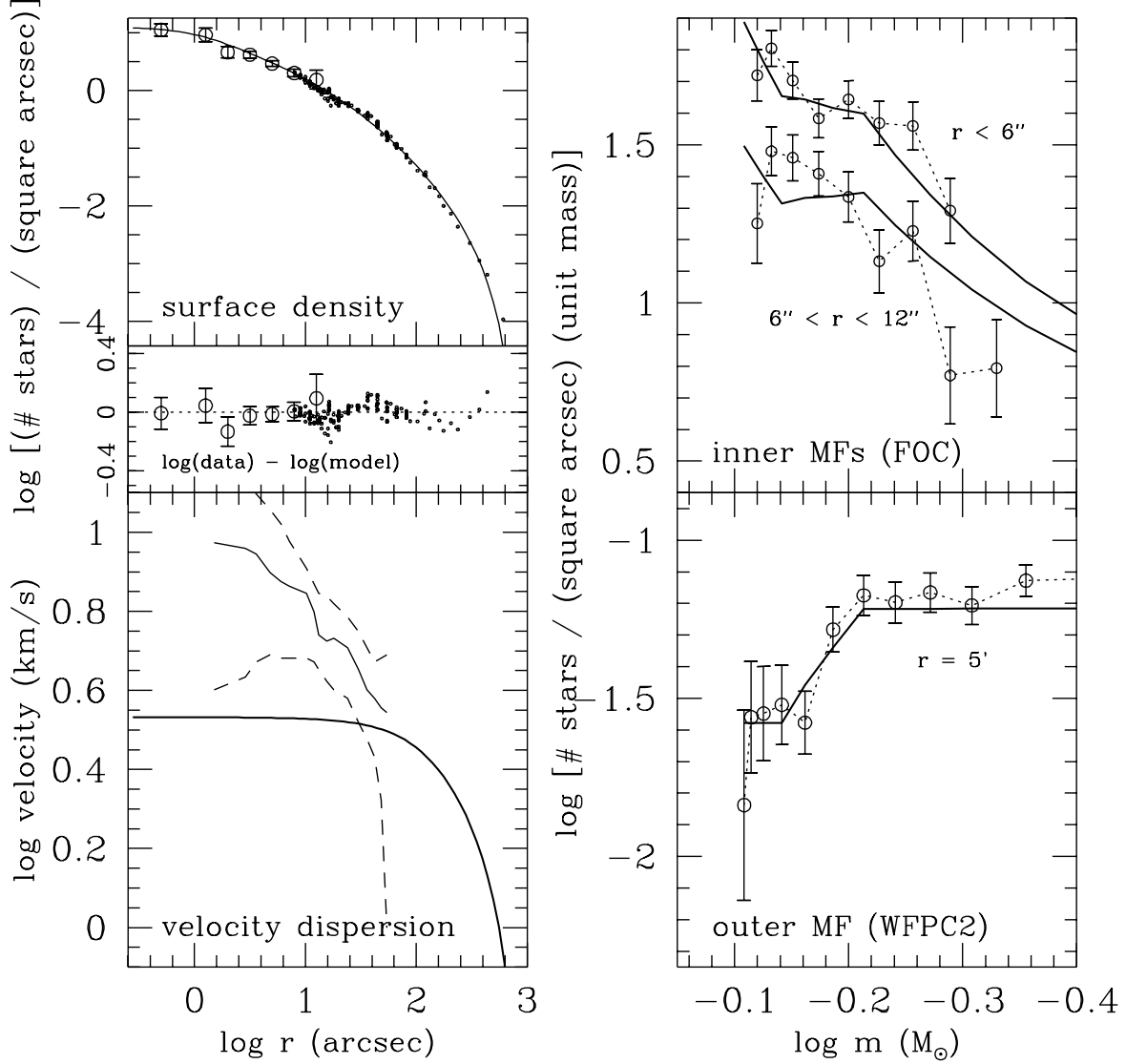
Figure 9. The King–Michie model, fit to our observations and to others from the literature. In all panels (except the lower left), points are observations, and solid lines are model constraints or predictions. (UL) The surface-density profile (model constrained to fit the observations). The large inner points are from this work; small outer points are from Trager *et al.* (1995). (LL) The velocity-dispersion profile. The narrow jagged line is the profile produced by Gebhardt *et al.* (1995) from a nonparametric analysis of their Fabry–Perot data. The dashed lines are their 90% confidence band on their profile. The heavier line is the profile predicted by our King model, which does not reproduce the central rise in velocity dispersion. (LR) The mass function at $r = 4\rlap{.}'6$ (model constrained to fit the data), from Piotto *et al.* (1996). (UR) Mass functions in the FOC fields, from this work (model matches the observed MFs).
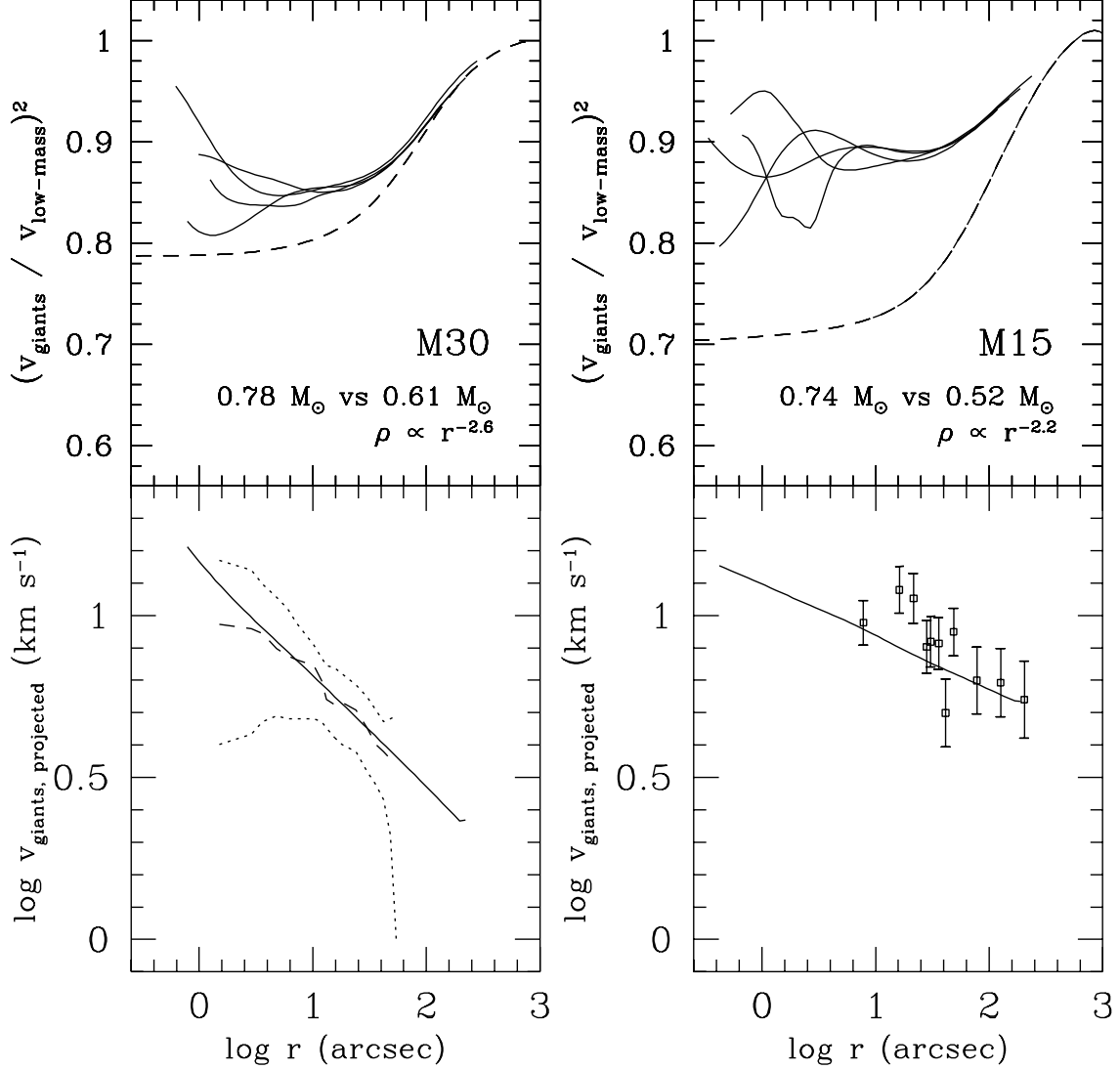
Figure 10.   The result of iteratively solving the Jeans equation (Eq. 2 in the text). Left panels refer to M30, and right panels refer to M15. *Lower panel on each side:* Line-of-sight velocity dispersion of giants, as found by solving the Jeans equation (solid lines), and as measured by Gebhardt *et al.* (1994, on the left, with the profile indicated by a dashed line, and its 90% confidence limits indicated by dotted lines), and by Gebhardt *et al.* (1995, on the right, indicated by points). The agreement with the observed VDPs shows that the potential being used in the solution of the Jeans equation is approximately correct. *Upper panel on each side:* Ratios of velocity dispersions of stars of differing mass, equivalent to either side of Eq. 3 (see text). The solid lines refer to the solution of the Jeans equation, using different numbers of iterations. The dashed lines show this velocity ratio for the King models described in this paper and in Paper I.